ENS DE LYON
Master Science de la matière
École Normale Supérieure de Lyon
Université Claude Bernard Lyon I

Lyon 1

Université de Lyon

Internship 2013–2014
Guilhem Poy
M2 Physics, Concepts and Applications

Shear Thickening in Dense Suspensions

Abstract: The rheological properties of two types of dense suspensions are explored. Repulsive suspensions of cornstarch in solution of water in glycerol are found to be shear thickening. The measured flow curves present features compatible with the recent theoretical idea of sigmoidal flow curves to explain shear thickening, which would implies the formation of vorticity bands and stress localisation. Attractive suspensions of cornstarch in oil shows interesting dynamic behaviour in Large Amplitude Oscillatory Shear experiments, with the mean viscosity increasing with the strain amplitude above 0.5. This increase is interpreted in terms of shear reversal and structures forming in the compression direction.

Keywords : *rheology, shear thickening, stress localisation, shear reversal, structures*

Internship supervised by:
Wilson Poon and Michiel Hermes
`w.poon@ed.ac.uk.fr` / tel. +44 (0) 131 650 5297
`m.hermes@ed.ac.uk` / tel. +44 (0) 131 650 5883
School of Physics & Astronomy, Institute for Condensed Matter and Complex Systems, Soft Matter Physics Group
The University of Edinburgh, Kings Buildings, James Clerk Maxwell Buildings, Mayfield Road, Edinburgh EH9 3JZ, United Kingdom
`http://www.ph.ed.ac.uk/`

August 18, 2014

Acknowledgements

I would like to thank Wilson Poon, for the support provided during this internship, Michiel Hermes, for the excellent advices given on an almost daily basis, Ben Guy, for the experimental tips that he kindly provided, and finally Mike Cates, for the fruitful discussions that we had about shear reversal and shear thickening. This was all in all a great experience and a real pleasure to work here at the university of Edinburgh during these last four months.

Contents

Introduction

Rheology is defined as the study of the flow of matter. One key physical quantity is the viscosity, which links the stress to the strain rate. More precisely, if we denote the velocity field of a sample by $\boldsymbol{v}(\boldsymbol{r})$, then the second-rank local strain rate tensor $\boldsymbol{E}$ is defined as

$$\boldsymbol{E} = \frac{1}{2}\left[\nabla \boldsymbol{v} + (\nabla \boldsymbol{v})^T\right]. \tag{1}$$

The Cauchy stress tensor $\boldsymbol{T}$ is then linked to the strain rate tensor by the contraction with the fourth-rank viscosity tensor $\boldsymbol{\eta}$ [5]

$$\boldsymbol{T} = 2\boldsymbol{\eta} : \boldsymbol{E}. \tag{2}$$

If only simple shear flow is studied, we can define the strain rate (or shear rate) $\dot{\gamma}$ as twice the component of the symmetric strain rate tensor in the plane of shear, and equivalently the shear stress as the component σ of the stress tensor in the same plane. Then the scalar viscosity η (simply denoted as viscosity in the following) is simply the ratio of shear stress over shear rate

$$\eta = \frac{\sigma}{\dot{\gamma}}. \tag{3}$$

When η is a pure constitutive constant, the material associated is called a Newtonian fluid. For more general materials, called complex fluids, the viscosity depends on the strain rate history. One particular class of complex fluids is the class of suspensions, constituted of particles in a fluid.

Although Einstein computed in 1906 the viscosity of rigid neutrally-buoyant spheres suspensions in the dilute regime [2], at this day no generic equation exists to explain the rheology of dense suspensions. At high volume fraction (also called packing fraction, and defined as the ratio of volumes $\phi = V_{\text{particles}}/\left[V_{\text{particles}} + V_{\text{fluid}}\right]$), one ultimately has to take into account the interaction and friction forces between the particles forming the suspension.

As these forces becomes relevant, interesting behaviours can appear in the rheology of suspensions. One of these interesting behaviours is shear thickening, which corresponds to an increase of the viscosity η with the strain rate $\dot{\gamma}$. This particular effect has some spectacular consequences: if the volume fraction is sufficiently high, one can run across a pool filled with a suspension of cornstarch in water, and yet sink in the same pool if staying at rest [1]; this is only possible because of a discontinuity of a few orders of magnitude in the function $\eta(\dot{\gamma})$, a phenomenon called Discontinuous Shear Thickening (DST). At lower packing fraction, one can still generally observe shear thickening, but with a smooth increase in the viscosity $\eta(\dot{\gamma})$, giving what we called Continuous Shear Thickening (CST). Recent theoretical work [11] suggests that shear thickening is due both to friction and finite interparticle repulsions: this repulsion sets a typical stress σ_{c}; when the stress σ is below σ_{c}, no frictional contacts are created and the viscosity is low, while above σ_{c}, frictional contacts proliferate and the viscosity becomes high.

Thus shear thickening seems to be a phenomenon relevant only in repulsive suspensions. But as it will be shown in this work, signatures of shear thickening can also be seen in Large Amplitude Oscillatory Shear (LAOS) experiments with attractive suspensions, if we accept a slightly modified definition: the mean viscosity during an oscillation of the stress or the shear rate is increasing with the amplitude of this oscillation. At first this seems absurd, because attractive suspensions possess a yield stress σ_{y}; when $\sigma < \sigma_{\text{y}}$, the attractive force cannot be overcome, and the suspension is solid-like, while above σ_{y}, the rheology of the suspension follows at equilibrium this generic law [7]

$$\sigma = \sigma_{\text{y}} + K\dot{\gamma}^n, \tag{4}$$

with $n \in]0,1[$, $\sigma_{\text{y}} > 0$ and $K > 0$. Therefore the viscosity $\eta = \sigma/\dot{\gamma}$ is expected to diverge at the yield stress and decrease with increasing strain rate. This decreasing is called shear thinning, the exact contrary of shear thickening. In fact, these laws are only valid in static experiments, when a constant shear rate or stress is applied and equilibrium is reached. In LAOS experiments, where the stress or strain rate is oscillating, the transient regime plays an essential role, and will be necessary to understand what is happening.

This report presents some experimental aspects linked to these phenomena. In the first part, I will present measurements of flow curves in shear thickening repulsive suspensions of cornstarch in solutions of water in glycerol. In the second part, I will explore the rheology of attractive suspensions of cornstarch in oil, with two types of measurement: LAOS experiment, to see the mean response of a sample submitted to an oscillatory shear, and shear reversal experiment, to analyse more precisely the transient response.

Part I
Suspensions with a repulsive force between particles

In this part, suspensions of cornstarch in a mixture of water and glycerol are studied. It is more challenging to use pure water, as it evaporates over time and thus changes the volume fraction of a sample. For a similar reason, pure glycerol is not a good choice, as it captures the water present in the air, and thus also modifies the volume fraction. By using solutions of water in glycerol, the influence of these two phenomena is limited. I have not tried to find the exact mass fraction needed to obtain an equilibrium, as it is likely that this equilibrium depends on the atmospheric conditions in the laboratory, but I have checked that with a ratio of mass $m_{\text{water}}/m_{\text{glycerol}}$ of roughly 0.5, the volume fraction of a suspension of cornstarch in this solution of water in glycerol was changing of approximately 1 % in 18 h, by measuring the mass of this sample over time. This was deemed acceptable, as all my experiments with these samples were conducted in less than eight hours. It should also be mentioned that the high viscosity of the glycerol slows down the sedimentation.

As water and glycerol are polar solvents, each particle of cornstarch possess a surface charge, which implies the creation of a layer of equal and opposite charge formed with the ions in solution. Thus, a long-range repulsive force is created between each particles. This mechanism is called the Helmholtz double layer model [8]. At short range, it is the collective London-Van Der Waals attractive forces between each molecules of the particles which dominates; this short-range attractive force is called the Hamaker force [6]. Lastly, frictional forces are present whenever there is a contact between two particles. Although more forces can be taken into account, these are the essential ingredients needed to understand the following.

The objective of this part is to measure experimentally the flow curve (the ensemble of points $(\sigma, \dot{\gamma})$ characterising a material) of these suspensions, and compare these results with the recent theoretical explanation of shear thickening with S-shaped curves proposed by Wyart and Cates [11]. In a first section, I will present how sigmoidal flow curves implies shear thickening, and what do we expect to measure with a given experimental setup. In a second section, I will present and discuss the results that I have obtained with suspensions of different volume fractions.

1 Theoretical considerations

1.1 S-shaped flow curves from a crossover of jamming densities

In [11], Wyart And Cates introduce the idea of a crossover between two types of rheology: a low pressure rheology, where the repulsive force is not overcome and the particles are frictionless (lubrication films don't break because of the repulsion), and a high pressure rheology, where the repulsive force is completely overcome and the particles are purely frictional. Here low pressure and high pressure corresponds to two limit cases: if we define P_c as the characteristic pressure scale fixed by the repulsive force and P as the particle pressure, then the frictionless rheology corresponds to $p = P/P_c \ll 1$, and the frictional rheology corresponds to $p \gg 1$. These two different regimes possess well-known phenomenological models, with a single dimensionless parameter $I = \eta_0\dot{\gamma}/P$ (η_0 is the viscosity of the solvent)

$$\phi = \Phi_{r,s}(I) \quad ; \quad \frac{\sigma}{P} = \mu_{r,s}(I). \tag{5}$$

In this equation and the following, subscript r corresponds to the frictional physics ("rough" particles) and subscript s corresponds to the frictionless physics ("smooth" particles). At fixed ϕ, these laws transform in a quasi-Newtonian scaling $P, \sigma \sim \eta_{r,s}\dot{\gamma}$, with a viscosity diverging at the jamming density ϕ_r for the frictional rheology and $\phi_s > \phi_r$ for the frictionless rheology

$$\eta_{r,s} = \frac{\lambda_{r,s}}{(\phi_{r,s} - \phi)^2}, \tag{6}$$

with $\lambda_{r,s}$ two constants homogeneous to a viscosity. Then, Wyart and Cates show that a crossover between these two physics is sufficient to obtain CST and DST. This crossover is parametrised by a second dimensionless parameter, the rescaled pressure p introduced earlier. Based on a microscopic argument and some simplifications, the following two-parameter model is then proposed

$$\frac{\sigma}{P} = \mu(I, p), \tag{7}$$

$$P = \frac{\lambda\dot{\gamma}}{(\phi_j(p) - \phi)^2} \Leftrightarrow \phi = \Phi(I, p), \tag{8}$$

$$\phi_{\mathrm{j}}(p) = f(p)\phi_{\mathrm{r}} + [1 - f(p)]\,\phi_{\mathrm{s}}. \tag{9}$$

Here, the p-dependant jamming density $\phi_{\mathrm{j}}(p)$ interpolates the two jamming densities $\phi_{\mathrm{r,s}}$ with the fraction of frictional contacts $f(p) \in [0,1]$. If $f(p)$ is assumed to converge quickly ($1 - f(p) = o\left(1/\sqrt{p}\right)$ is a sufficient condition), then sigmoidal curves arise in an interval $[\phi_{\mathrm{dst}}, \phi_{\mathrm{r}}]$ below ϕ_{r}. A sigmoidal (or S-shaped) flow curve $\{(\sigma(s), \dot{\gamma}(s))\,; s \in [0, +\infty]\}$ (s is an arbitrary variable parametrizing the curve) is a double-stress curve which possesses a central part with a negative slope $d\sigma/d\dot{\gamma} < 0$, and two Newtonian plateaus at low and high stress. A Newtonian plateau is a part of the curve where the material is Newtonian-like, i.e. where $\sigma(s)/\dot{\gamma}(s)$ is locally constant and positive. Below ϕ_{dst}, the flow curve is single-valuate in the stress, while between ϕ_{r} and ϕ_{s}, the upper branch of the sigmoid curve disappears. The Figure 1 presents these different cases, obtained for $\phi_{\mathrm{r}} = 0.58$, $\phi_{\mathrm{s}} = 0.64$ and $f(p) = 1 - \exp(-p)$. If we assumed as a simplification that $\mu(I,p) \simeq \mu(\phi)$, then the flow curve has the same shape at fixed ϕ as the curve $(p, \dot{\gamma})$, and thus Figure 1 gives the different types of flow curves, modulo a multiplicative factor.

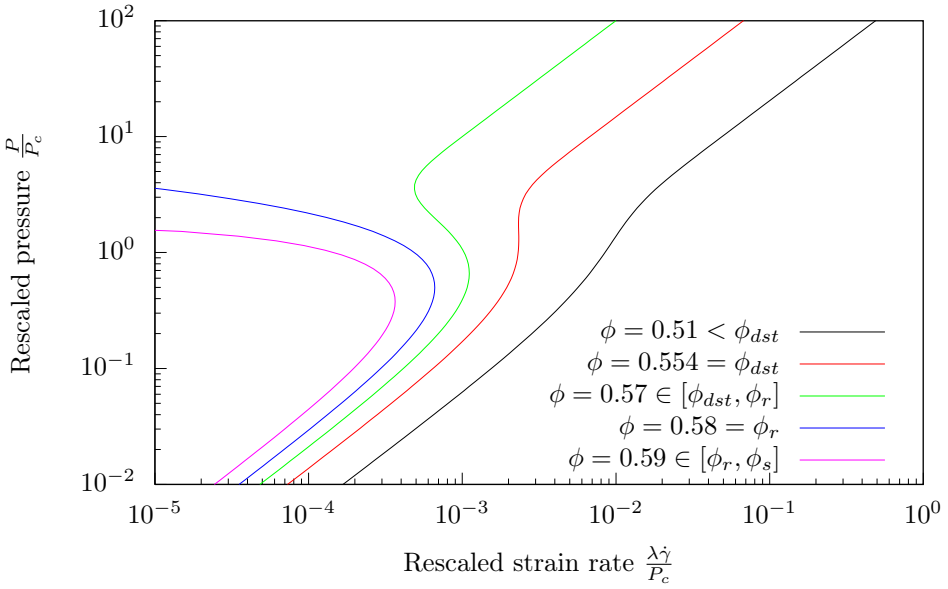

Figure 1: Curves $(p, \dot{\gamma})$ obtained for different packing fractions with $\phi_{\mathrm{r}} = 0.58$, $\phi_{\mathrm{s}} = 0.64$ and $f(p) = 1 - \exp(-p)$. Growing ϕ corresponds to decreasing $\dot{\gamma}$.

It can easily be shown that a linear velocity profile (i.e. constant strain rate) is unstable when $d\sigma/d\dot{\gamma} < 0$ [7]. Therefore, we need to investigate how a sample with a sigmoidal flow curve responds to an applied shear stress or shear rate. At fixed shear rate, we expect to observe discontinuous jumps and hysteresis: if we start from a very low $\dot{\gamma}$ and increase it, we will measure a continuous increase of σ until $d\dot{\gamma}/d\sigma = 0$ (the right vertical tangent of the sigmoidal curve) and then a discontinuous jump followed again by a continuous increase; if we start from a very high $\dot{\gamma}$ and decreases it, we will measure a continuous decrease of σ until $d\dot{\gamma}/d\sigma = 0$ (the left vertical tangent of the sigmoidal curve) and then a discontinuous jump followed again by a continuous decrease. This behaviour has been observed experimentally, according to [11]. At fixed stress, the answer is a little more complex as the central part of the flow curve is unstable; this will be the topic of the next subsection.

1.2 Sigmoidal flow curves and mean stress control

If we try to apply a shear stress $\sigma(s^*)$ with $d\sigma/d\dot{\gamma}(s^*) < 0$, we know that the velocity profile associated with $\dot{\gamma}(s^*)$ is unstable. If so, what is the equilibrium state reached by the sample? This situation is somewhat similar to the liquid-gas transition, where the isotherm (P, V) can possess a thermodynamically unstable part where $dP/dV > 0$; in this case, the stable solution is found by minimizing the free energy, which yields a coexistence between one low-volume state (the liquid) and one high-volume state (the gas). By analogy, we can try to construct a state where two different stress states coexist at the same shear rate: one high stress on the upper branch of the sigmoidal curve, and one low stress on the lower branch. The problem here is that we do not have a magical tool like the free energy to say which common strain rate will be selected. For the sake of the demonstration, we will choose an arbitrary strain rate $\dot{\gamma}^*$ at which the coexistence happens, but let's keep in mind that there is no fixed rule to compute this $\dot{\gamma}^*$.

The Figure 2 sketches the coexistence in an ideal situation: the shear plane is (xz) and the mean stress σ_{exp} is applied globally by the upper plate of surface $S = WL$; periodic boundaries are chosen along the direction x, and the free surfaces parallel to the shear plane (xz) are supposed to be perfectly flat (no boundary effects).

At the coexistence, the experimental measured shear rate is $\dot{\gamma}^*$, and the stress reorganises locally in two bands, with the interface orthogonal to the vorticity direction (the direction of the curl of the velocity field). The size of these bands, called vorticity bands, is fixed by the imposed mean stress

$$\sigma_{\text{exp}} = \frac{\sigma_+ S_+ + \sigma_- S_-}{S} = r\sigma_+ + (1-r)\sigma_-, \tag{10}$$

where $S_+ = rLW$ and $S_- = (1-r)LW$ are the surfaces occupied by the two bands.

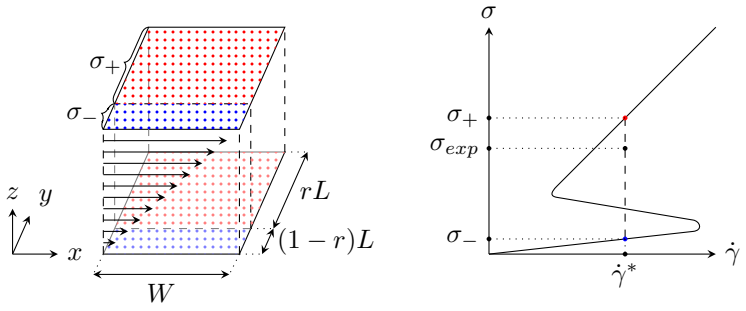

Figure 2: Vorticity bands developing during the coexistence interval $[\sigma_-, \sigma_+]$. The boundaries parallel to (yz) are periodic, and the boundaries parallel to (xz) are flat interfaces. The mean stress σ_{exp} is applied by the upper plate, while the lower plate stays fixed. x is the velocity direction (the direction of the velocity field), y is the vorticity direction (the direction of the curl of the velocity field) and z is the gradient direction (the direction of the gradient of the velocity field)

Obviously, such an ideal setup is not relevant in real experiment. During my internship, I have mostly worked with a plate-plate geometry mounted on a stress-control rheometer. The Figure 3 represents this geometry: the mean stress is applied by the rotating upper circular plate, while the lower plate stays fixed; the gap h_{p} can be set by moving the system {*motor; shaft; upper plate*} vertically; finally, hatched plates are used to limit wall slip.

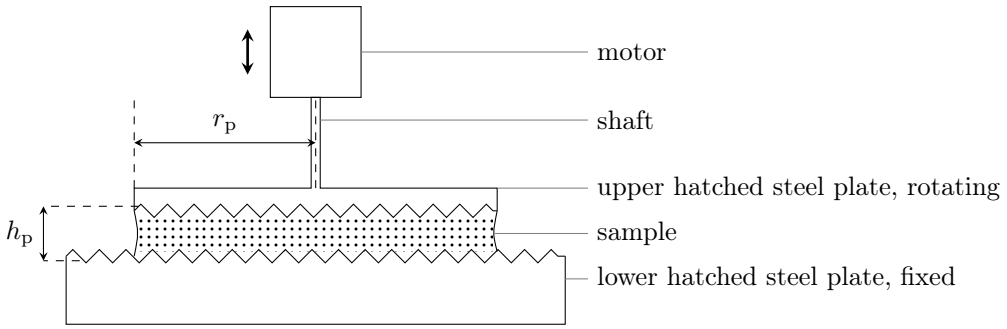

Figure 3: The plate-plate geometry used. The motor can move vertically allowing to set the gap h_{p}. The stress is applied by the rotating upper circular plate.

The main difference with the previous ideal situation is that the shear rate is not constant along the vorticity direction (radial direction): the strain rate increases linearly from 0 at the center of the plate to a certain value at the maximal radius $r = r_{\text{p}}$. Thus, if there is a coexistence between two states as before, these states cannot be pure-stress states, but rather intervals of stresses. I have depicted the expected band structure in the Figure 4.

We need to consider how the stress and the shear rate are applied in this geometry, as these two quantities are not constant across the sample. What is really applied is the torque Γ of the motor, and what is really measured is the angular velocity Ω of the upper plate. By integrating the local stress times the radius along the surface of the upper plate, we obtain the torque

$$\Gamma = \int_0^{r_{\text{p}}} \sigma(r) r \cdot 2\pi r \mathrm{d}r. \tag{11}$$

If we assume that the lower and upper branches of the sigmoidal flow curves are perfect Newtonian plateaus of viscosities η_- and η_+, as depicted in Figure 4, then the local stress is expressed as the local stress

$$\sigma(r) = \begin{cases} \eta_- \dot{\gamma}_{\text{o}} \frac{r}{r_{\text{p}}} \ , \ r < r_{\text{i}} \\ \eta_+ \dot{\gamma}_{\text{o}} \frac{r}{r_{\text{p}}} \ , \ r \in [r_{\text{i}}, r_{\text{p}}] \end{cases} \ , \tag{12}$$

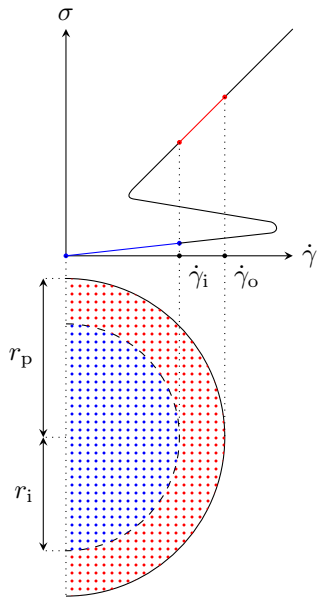

Figure 4: The structure of the vorticity band in the plate-plate geometry. The two degrees of freedom during the coexistence are the position of the interface and the strain rate at the edge

with r_i the radial position of the interface between the two bands and $\dot{\gamma}_\mathrm{o}$ the strain rate at the edge of the sample. By injecting this expression in the equation 11, we obtain

$$\Gamma = \frac{\pi \dot{\gamma}_\mathrm{o} r_\mathrm{p}^3}{2} \left\{ \eta_- + (\eta_+ - \eta_-) \left[1 - \left(\frac{r_\mathrm{i}}{r_\mathrm{p}} \right)^4 \right] \right\}. \tag{13}$$

The software used to communicate with the rheometer defines in the plate-plate geometry the experimental stress as

$$\sigma_\mathrm{exp} = \frac{2\Gamma}{\pi r_\mathrm{p}^3}, \tag{14}$$

and the experimental strain rate as

$$\dot{\gamma}_\mathrm{exp} = \frac{r_\mathrm{p}\Omega}{h_\mathrm{p}} = \dot{\gamma}_\mathrm{o}. \tag{15}$$

Therefore, we obtain our final expression of the experimental stress

$$\sigma_\mathrm{exp} = \dot{\gamma}_\mathrm{exp} \left\{ \eta_- + (\eta_+ - \eta_-) \left[1 - \left(\frac{r_\mathrm{i}}{r_\mathrm{p}} \right)^4 \right] \right\}. \tag{16}$$

When there is only the low-stress band ($r_\mathrm{i} = r_\mathrm{p}$), we retrieve the Newtonian scaling $\sigma_\mathrm{exp} = \eta_- \dot{\gamma}_\mathrm{exp}$, and when the high-stress band invades most of the sample ($r_\mathrm{i} \to 0^+$), we retrieve the quasi-Newtonian scaling $\sigma_\mathrm{exp} \simeq \eta_+ \dot{\gamma}_\mathrm{exp}$ (the low-stress band is always present because the strain rate always starts from 0 at the center of the plate). While approximative (we will see that the lower and upper branches of the flow curves are not perfectly Newtonian), this equation will be handy to interpret some of the experimental data.

In any case, we can remember the following generic argument: with the ideal situation of the Figure 2, the only degree of freedom was the common strain rate $\dot{\gamma}^*$, while with the plate-plate geometry, we have two degrees of freedom: the position of the interface r_i and the strain rate at the edge $\dot{\gamma}_\mathrm{o}$. For now, this seems like a complication to interpret the experimental data, but we will see in the next section that in fact, these two situations should give similar results, at least at the beginning of the coexistence.

2 Measurement of the flow curve

2.1 Experimental setup and protocol

I now present the experimental setup and protocol used to measure experimentally a flow curve. The plate-plate geometry represented in Figure 3 was mounted on an Advanced Rheometer 2000 (TA Instruments). This rheometer uses an air bearing to limit any friction in the rotation of the upper plate; a desiccant dryer PNEUDRI MiDAS (Parker) was used to keep the air dry inside this air bearing. The interface between the rheometer and

the laboratory computer was made with an old version of the closed-source software Rheology Advantage (TA Instruments v5.2.2). Data coming from this software was parsed and converted to a usable format by a custom Perl script that I have written at the beginning of my internship, and then processed by Octave scripts to allow treatment and visualisation of the signals.

To get a functional feedback between the angular velocity and the torque, the rheometer needs to be calibrated: first the moment of inertia of the air bearing only (i.e. without any shaft and plate mounted on it) is calibrated by measuring the angular velocity after applying a constant torque, then the moment of inertia of the system {*shaft; upper plate*} is calibrated using the same method, and finally the friction of the air bearing is calibrated by measuring the angular velocity right after stopping a high applied torque. The annexes 1 and 2 describes in detail how these calibrations works.

To convert the torque and angular velocity in respectively stress and strain rate with the equations 14 and 15, the rheometer also needs the values of r_p and h_p. I have used a circular upper plate of radius $r_\mathrm{p} = 20$ mm and a gap between the two plates of $h_\mathrm{p} = 1$ mm. The gap was calibrated using the pressure plate included in the rheometer below the lower plate: by measuring the pressure on the lower plate while slowly lowering the upper plate, the rheometer can calibrate precisely the contact between the two plates; once this reference is known, the gap can be fixed automatically by the software.

The samples were made using distilled water, glycerol from Fisher Chemical (G/0600/17), and cornstarch from Sigma-Aldrich (S4126). The protocol used is the following: first, a solution of water in glycerol GLW is made and its density ρ_glw measured with a density meter DMA 4500 (Anton Paar); each of these solutions was found to have a density around 1.17 g/m^3; to limit the change in density due to the absorption or evaporation of water, these solutions were used only in the 8 hours following their creation. Then, the suspension is made by measuring the added mass m_cf of cornstarch and m_glw of GLW. The volume fraction is finally computed using

$$\phi = \frac{m_\mathrm{cf}/\rho_\mathrm{cf}}{m_\mathrm{cf}/\rho_\mathrm{cf} + m_\mathrm{glw}/\rho_\mathrm{glw}}. \tag{17}$$

The calibration of the density of the cornstarch is described in detail in annexe 3, and was found to be $\rho_\mathrm{cf} = 1.45 \pm 0.004$ g/cm^3.

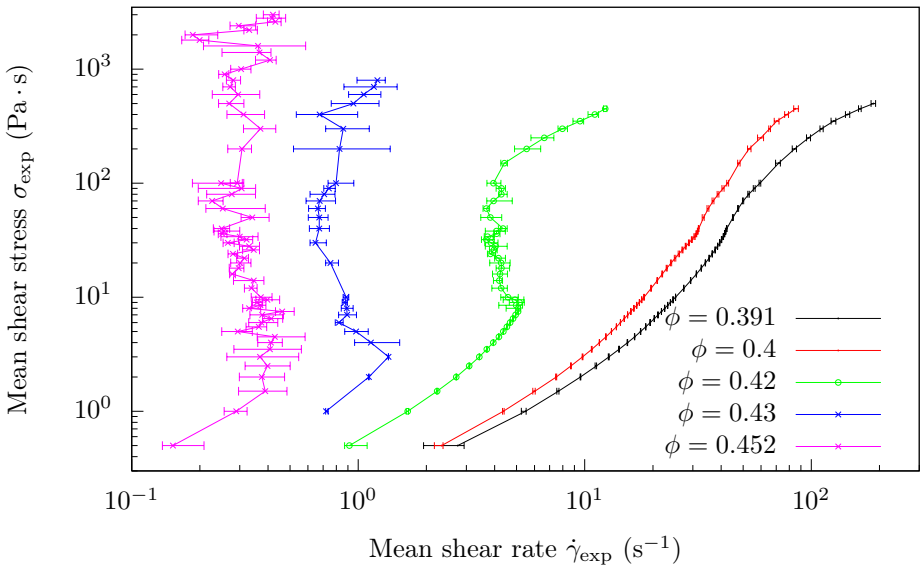

Figure 5: Flow curves obtained when measuring an ascendant sweep immediately after loading the sample in the geometry. Growing volume fractions correspond to decreasing strain rate. Each point correspond to an average over the last 6 s of the peak hold, and the error bars corresponds to the minima and maxima of each peak hold.

The created suspension is then loaded in the gap zone of the geometry, by first spreading the sample on the lower plate, and then lowering the upper plate to the gap altitude h_p. The part of the sample in excess outside the gap zone is then removed using a spatula (this is very easy to do due to the shear thickening). The software does not allow much control over the protocol used in an experiment, so I chose the most manual method available: a series of peak hold were applied at successive stresses. Here, a peak hold is defined as a measurement of the strain rate when a constant stress is applied. Each of these peak hold lasts 8 s, and 40 points are measured at fixed increments of time during this period; this sample rate is the maximum allowed by the serial connection without having delay problems. In fact, there is a fast sampling option, but the problem

with this mode is that during the transfer of the data ($\sim$ 1 min), the stress continues to be applied, and can destroy the sample quickly when this stress is sufficiently high, as it will be seen in the next subsection. An ensemble of peak holds associated with increasing stresses (respectively decreasing stresses) will be designated as *ascending sweep* (respectively *descending sweep*). For each peak hold, the experimental stress σ_{exp} is simply the applied stress, the strain rate $\dot{\gamma}_{\text{exp}}$ is estimated as the mean of the last 6 s of the temporal series of measured strain rates (the 30 last points), and the error bar is computed from the minimum and maximum values of the same cut temporal series (this allows a quick visualisation of the stability of the signal after that the feedback has set the stress to the desired value).

2.2 Results

I now present the flow curves obtained for different packing fractions and protocols. To easily interpret the flow curves in log-log scale in terms of viscosities, it should be kept in mind that a line of slope 1 corresponds to a Newtonian plateau and the higher this line is, the higher the viscosity is (this follows directly from the relation $\log_{10}[\sigma] = \log_{10}[\eta] + \log_{10}[\dot{\gamma}]$).

The Figures 5 and 6 show the very first ascending sweeps measured on samples with different volume fractions directly after the loading, by respectively plotting σ against $\dot{\gamma}$ and η against $\dot{\gamma}$. The error bars are only present in Figure 5, as Figures 5 and 6 are just two different ways of representing the same data. We can see three different classes of flow curves: the first one, at packing fractions lower than $\phi^*_{\text{dst}} = 0.41 \pm 0.005$ (the first two curves starting from the right), corresponds to CST, with a continuous increase of the viscosity with the strain rate. The stability of the signal is excellent for each point of the flow curve.

The second type of flow curves is obtained for packing fractions ranging from ϕ^*_{dst} to $\phi^*_{\text{r}} = 0.425 \pm 0.005$ (the third curve), and presents one low-viscosity Newtonian plateau, quite stable, one vertically ascending part, where the stress and viscosity increase at roughly the same strain rate with an important noise, and one high viscosity Newtonian plateau, slightly noisy.

Finally, the third type of flow curves is obtained for packing fractions greater than ϕ^*_{r} (the first two curves starting from the left), and is basically the same as the second class of curves except that there seems to be no high-viscosity plateau, or at least not at the same stress than the other curves (the Newtonian plateau for the two first classes is always reached around $\sigma_{\text{exp}} = 400$ Pa).

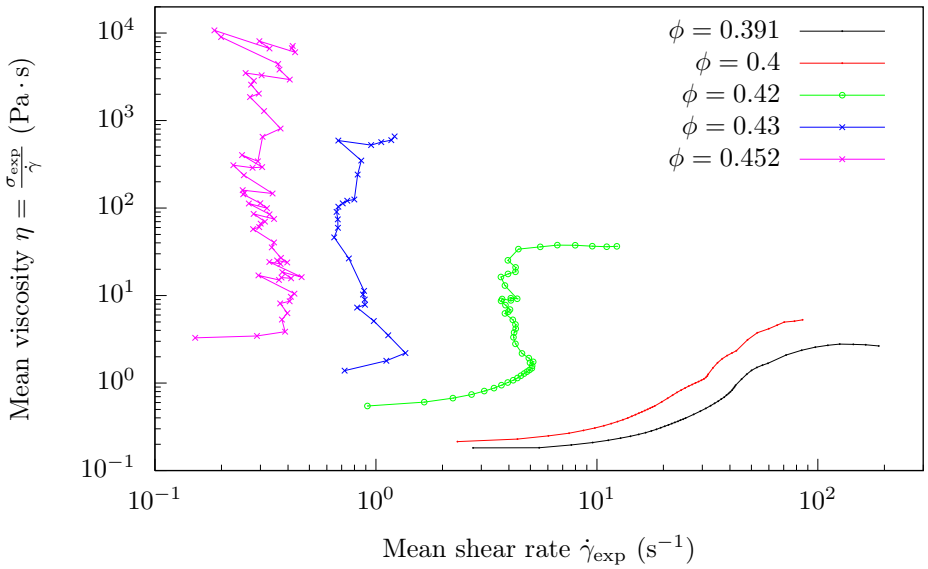

Figure 6: Same data as the Figure 5, except that it is the viscosity which is plotted against the strain rate

The data obtained on Figures 5 and 6 are reproducible over different samples if the measurement is done immediately after the loading and quickly (no longer than $\sim$ 8 min for the whole ascending sweep). For packing fraction lower than ϕ^*_{r}, if the high Newtonian plateau is reached in the first series of peak hold, then things deteriorate immediately after, and measurements are not reliable. If on the contrary the first ascending sweep is stopped in the shear thickening regime (the vertical part of the measured flow curve), then the sample deteriorates only after a few other measurements (typically 3).

This last statement is visible on Figure 7, where successive ascending sweeps were applied on a fresh sample of volume fraction 0.43, with each ascending sweep stopping at a lower stress 90 Pa. We clearly see the strain rate becoming very noisy at one point, and decreasing until a mean value is reached around 0.6 s^{-1}. This value

of mean strain rate is consistent for the first three ascending sweeps made on that sample, but after that, any measurements were shifted to higher strain rate and became even more noisy.

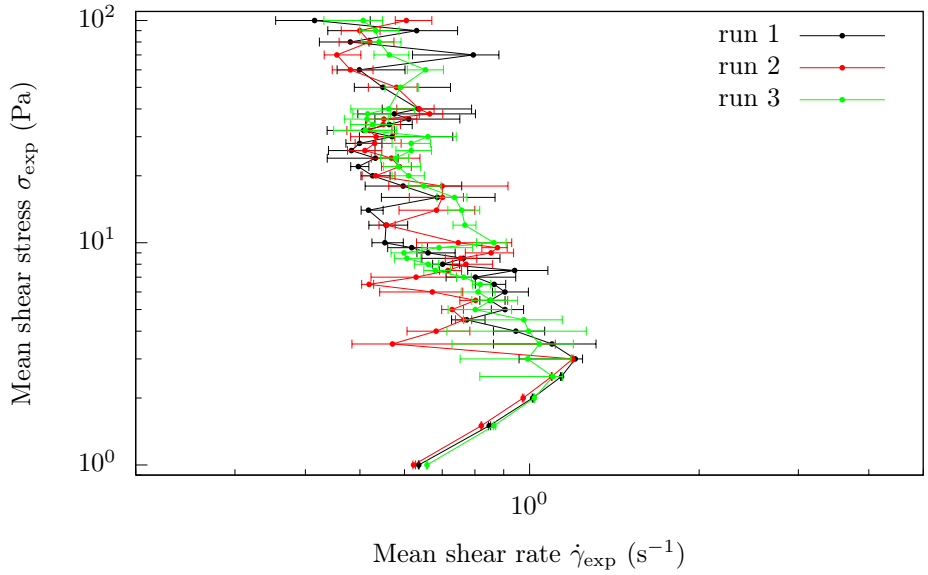

Figure 7: Partial flow curves measured with a volume fraction of 0.43. Ascendant sweeps with stresses ranging from 1 Pa to 90 Pa were successfully measured on the same sample, without reloading between each sweeps.

In Figure 8 I show what happens when we measure a descending sweep immediately after an ascending sweep. The same behaviour was observed on different samples with different packing fractions between ϕ^*_{dst} and ϕ^*_r, and also by changing the maximum stress applied (providing that this stress is in the high Newtonian regime). This strong hysteresis is somewhat the most disturbing result, and will be analysed in length in the next subsection.

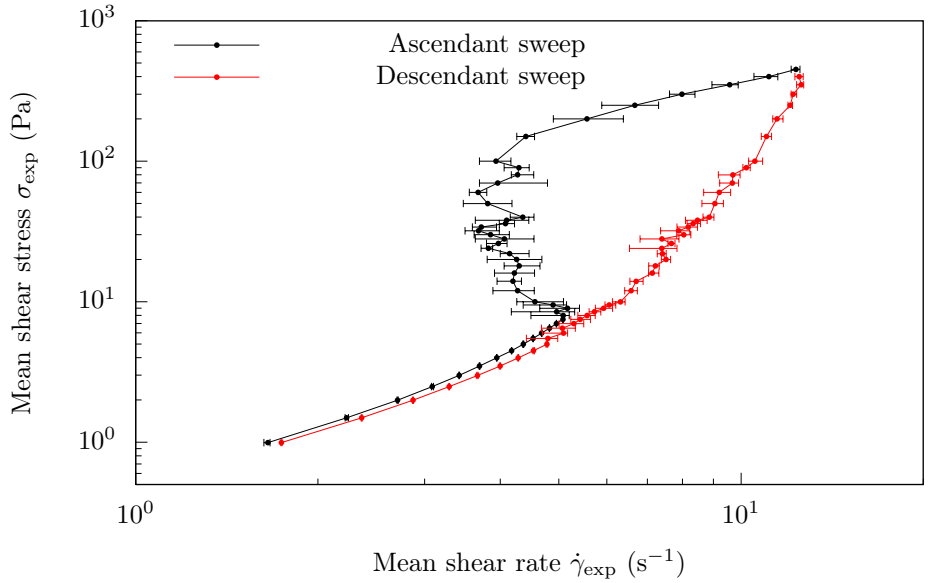

Figure 8: The ascending and descending sweeps obtained for a volume fraction of 0.42. The ascending sweep corresponds to the left curve, the descending sweep corresponds to the right curve

I have not used any imaging techniques, but I can at least provide a basic description of the edge of the sample. For volume fraction lower than ϕ^*_{dst}, the interface starts by being a perfect meniscus in the low Newtonian plateau. During the shear thickening, a periodic wave pattern along the angular direction appears on the surface. The amplitude of the waves increases with the stress, and ultimately the pattern breaks when the high-viscosity plateau is reached: the waves are replaced by blobs of dispersion sticking through the interface, rolling around the edge of the samples.

For volume fraction between $\phi^*_{\rm dst}$ and $\phi^*_{\rm r}$, the interface is stable in the low Newtonian regime, and stays so until the end of the shear thickening regime. When the high-viscosity plateau is reached (for a stress of approximately 400 Pa), discrete blobs of sample appear across the edge and the interface can no longer be defined in a continuous manner after this destabilisation.

Finally, for volume fraction above $\phi^*_{\rm r}$, these blobs are also observed for stresses above 400 Pa, but as the stress continue to increase, cracks start to appear around 2000 Pa, which could imply wall slip.

2.3 Discussion

Some properties of my results seem to be compatible with the idea of a sigmoidal curve, but caution is needed to interpret the measured flow curves. For the first type of measured flow curves (below $\phi^*_{\rm dst}$, continuous increase of $\sigma_{\rm exp}$ with $\dot\gamma_{\rm exp}$, well-defined high-viscosity plateau), a continuously shear thickening flow curve would indeed yields a continuous measured flow curve, because the stress and strain rate can increase continuously from the center of the plate to the edge without having to create any discontinuous bands. However, no explanation has been found for the periodic pattern appearing on the edge, and why this pattern disappears at higher volume fraction.

It is more tricky to interpret the second type of flow curves (between $\phi^*_{\rm dst}$ and $\phi^*_{\rm r}$, discontinuous increase of $\sigma_{\rm exp}$ with $\dot\gamma_{\rm exp}$, well-defined high-viscosity plateau). At low stresses, the stable continuous increase of $\sigma_{\rm exp}$ with $\dot\gamma_{\rm exp}$ is compatible with a single band exploring the lower branch of a sigmoidal flow curve. However, the viscosity in this regime is not perfectly constant but increases continuously with the strain rate, which means the equation 16 is only approximate (the low stress regime is not a perfect Newtonian plateau). After this stable regime, the experimental strain rate suddenly becomes much more noisy and decreases until a mean value is reached, yielding a continuous increase of the experimental stress at a fixed strain rate. According to the approximate equation 16, this is possible with keeping $\dot\gamma_{\rm exp}$ fixed while nucleating a high-stress band near the edge ($r_{\rm i}/r_{\rm p} < 1$). At this point, two important remarks should be made concerning the equation 16: the factor $[\eta_+ - \eta_-]$ is at least one order of magnitude greater than η_- (for example at $\phi \simeq 0.42$, we have $\eta \simeq 2.6$ Pa$\cdot$s just before the signal become noisy and $\eta \simeq 68$ Pa$\cdot$s for the well-defined high viscosity plateau), and the structure factor $\left[1 - (r_{\rm i}/r_{\rm p})^4\right]$ varies very quickly with the position of the interface between the two bands $r_{\rm i}$. These two remarks implies that a little change in $r_{\rm i}$ gives a big change in the measured stress $\sigma_{\rm exp}$. For example, if we choose $\eta_- \simeq 2.6$ Pa$\cdot$s and $\eta_+ \simeq 68$ Pa$\cdot$s at $\phi \simeq 0.42$, we have $(\eta_+ - \eta)/(\eta_+ - \eta_-) = 0.5$ for only $r_{\rm i}/r_{\rm p} \simeq 0.84$. This means that during at least the first half of the coexistence, the high-stress band is concentrated on the edge of the sample and is very thin. Finally, the high-viscosity plateau observed would be compatible by keeping $r_{\rm i}$ fixed while increasing the strain rate $\dot\gamma_{\rm exp}$. The reproducibility of this plateau across different samples and the fact that it always begins at the same stress of roughly 400 Pa seem to indicate that it is not due to an experimental artefact (wall slip or other). However, some gap size effects were found lately during the redaction of this report (Ben Guy, private communication), which would indicate that this apparent plateau is not a perfect Newtonian plateau: when the gap size increases, Ben found that the high-viscosity plateau is shifted to higher viscosities at fixed stress. Nevertheless, the main features of the model of Wyart and Cates is verified, namely that the high-viscosity plateau always appears at the same stress (which is equivalent to the pressure scale $P_{\rm c}$ assuming that the global friction coefficient $\mu = \sigma/P$ does not change much with the volume fraction; this is a reasonable assumption considering the range of packing fractions studied).

The last type of flow curves (above $\phi_{\rm r}$, increase of $\sigma_{\rm exp}$ at fixed $\dot\gamma_{\rm exp}$, no well-defined high-viscosity plateau) is the most difficult to interpret. Indeed, the continuous increase of the stress $\sigma_{\rm exp}$ at a mean fixed strain rate $\dot\gamma_{\rm exp}$ is very similar to the second type of flow curves, but this time there is no high-viscosity plateau around 400 Pa. This is certainly consistent with the fact that the upper branch of the sigmoidal curve disappears in the model of the previous section, but it does not tell us in this case what the structure of stress inside the sample is. The increase at fixed strain rate seems to indicate that there is still a band structure in the sample, but if this is true the origin of the new high-stress branch is unknown. Furthermore, the cracks appearing on the edge at very high stress would indicate that we have to take into account additional effects.

As for the strong hysteresis observed when measuring successively an ascendant and descendant sweep, this can be interpreted as the following process: when the stress starts to decrease after the high-viscosity plateau, $\dot\gamma_{\rm exp}$ decreases and $r_{\rm i}/r_{\rm p}$ increases simultaneously, which yields the smooth decrease observed in Figure 8. This hysteresis is therefore due to the fact that there is two degrees of freedom $\dot\gamma_{\rm exp}$ and $r_{\rm i}$: while during the ascendant sweep, only one variable varies at a time ($r_{\rm i}$ during the shear thickening regime, $\dot\gamma_{\rm exp}$ when the high-viscosity plateau is reached), during the descendant sweep both variables vary, for an unknown reason. This process only shows that the hysteresis is not incompatible with a sigmoidal flow curve, but it does not give any physical meaning for this hysteresis.

As a final note, after discussions with Michiel Hermes and Mike Cates, a possible origin of the irreversible alteration of samples has been found: the high-stress band corresponds to a high particle pressure and the low-stress band to a low particle pressure, therefore we should expect a gradient in particle density to form, with

a high density in the center and a low density at the edge of the plate. This gradient should alter the sample irreversibly, but it is not very clear how the measured flow curves are altered in the plate-plate geometry. Ultimately, it would give equal pressure inside the sample, with a frictional high-concentration band and a frictionless low-concentration band. This gradient banding has apparently been observed by A. Lemaître, but the only information about that was an abstract get by a private communication (Macroscopic Discontinuous Shear Thickening vs Local Shear Jamming in Cornstarch). In any case, the transition between vorticity banding and gradient banding is expected to be complicated, and imaging techniques are certainly needed.

In conclusion, my experimental results do not show any contradictions with the idea of a sigmoidal curve to explain shear thickening, and verify some of the features of the model developed by Wyart and Cates: two characteristic volume fractions are found, associated with qualitative change in the measured flow curve; the high-viscosity plateau, when defined, always appears at the same stress; the increase of the viscosity at fixed strain rate is compatible with a sigmoidal flow curve assuming stress localisation in bands. Ultimately, imaging techniques should be used to determine more precisely how the flow evolutes with the stress and the time, which is one of the future project of the Soft-Matter team of the university of Edinburgh.

Part II
Suspensions with an attractive force between particles

In this part, suspensions of cornstarch in oil are studied. Contrarily to water and glycerol, there is no ions in solution in the oil. As a consequence, the particles of cornstarch does not acquire a surface charge and there is no repulsive force, although there is still the Hamaker attractive force and the friction force. Because of this dominant short-range attractive force, we expect these suspensions to possess a yield stress σ_y, characteristic stress scale above which the suspension can flow with a finite viscosity and below which the viscosity diverges with the time.

This definition of the yield stress is essential, because below σ_y, the suspension is never totally jammed, and continues to flow (more and more slowly). This allows to do LAOS and shear reversal experiments with a stress below σ_y, and still measuring an interesting rheological response. The objective of this part is to present a shear thickening-like behaviour when doing LAOS experiments, and interpret this shear thickening in terms of shear-reversal and structures. The first section will be dedicated to Large Amplitude Oscillatory Shear experiments, and the double scaling of the viscosity. The second section will be dedicated to the transient rheological response during a reversal of the direction of shear, and the interpretation in terms of structures. This interpretation will be useful to interpret the LAOS results under a more generic framework.

1 Large Amplitude Oscillatory Shear approach

In LAOS experiment, a sample is submitted to a sinusoidal stress or strain of a certain amplitude, which can be *large*. *Large* means that the measured conjugated quantity (stress if strain-control, strain if stress-control) is not necessarily sinusoidal, i.e. we do not restrain ourselves to the linear regime, where both quantities are sinusoidal. As stress-control is the mode giving the best feedback with the rheometer that I have used, all experiments in this section were conducted by imposing a sinusoidal stress of a fixed amplitude σ_0 and angular frequency ω

$$\sigma(t) = \sigma_0 \sin(\omega t). \tag{18}$$

Once this sinusoidal stress is applied, the strain is measured in function of the time, and yields after a transient regime a periodic function $\gamma(t)$ of period $2\pi/\omega$ and amplitude γ_0. Then, the mean elastic modulus is defined as [3]

$$G_1' = \frac{\omega}{\pi\gamma_0^2} \oint \sigma(t)\gamma(t)\mathrm{d}t, \tag{19}$$

and the mean loss modulus as

$$G_1'' = \frac{1}{\pi\gamma_0^2} \oint \sigma(t)\dot{\gamma}(tr)\mathrm{d}t. \tag{20}$$

Therefore, G_1' is characteristic of an Hookean behaviour, where the strain deformation is in phase with the stress, and G_1'' is characteristic of a viscous behaviour, where the strain rate is in phase with the stress. This last quantity is often reinterpreted in terms of the mean viscosity $\eta_1' = G_1''/\omega$. The objective of this section is to find the scaling of this viscosity with the amplitude of the shear, the frequency, and the volume fraction.

1.1 Experimental protocol

The same experimental setup of part 1 was used, only the protocol was changed. Two different sources of cornstarch were used: the same cornstarch as before (S4126, Sigma-Aldrich), and cornstarch from the chain of supermarket Sainsbury's. The calibration of the density of these cornstarches (described in the annexe 3) has given the same results within the precision of the measurement: $\rho_{\text{cf}} = 1.45 \pm 0.004$ g/cm^3. The samples are prepared by measuring and mixing a mass m_{cf} of cornstarch and m_{oil} of oil; the volume fraction is deduced from

$$\phi = \frac{m_{\text{cf}}/\rho_{\text{cf}}}{m_{\text{cf}}/\rho_{\text{cf}} + m_{\text{oil}}/\rho_{\text{oil}}}, \tag{21}$$

with $\rho_{\text{oil}} = 0.920$ g/cm^3 measured with the same density meter as before (DMA 4500, Anton Paar).

Once the sample loaded in the geometry and the surplus removed with a spatula, the following protocol is used with the Rheology Advantage software:

1. A frequency ω is chosen
2. A descendant amplitude sweep is measured, at the angular frequency ω and from the stress amplitude σ_{start} to the stress amplitude σ_{end}. These two values of stress are chosen in order to obtain strain amplitudes ranging from 10^{-1} to 10^2. Each step of the sweep (at one fixed amplitude) consist of a conditioning part of 5 oscillation cycles, and a sampling part of 5 cycles. A generic parameter of 15 steps per stress decade is chosen.
3. The mirrored ascendant amplitude sweep, from σ_{end} to σ_{start}, is measured using the same generic parameters.
4. A new frequency is chosen and we start again from 2.

The frequencies used were $\omega = 4, 5, 6, 7, 8, 9, 10$ rad/s. Although it is possible to get the temporal series of measured strain and applied stress, the procedure to get them is so horrible (it involves a long process of selecting each points of a curve, activating obscure options, and make copy/paste via excel) that I preferred to use the values of G_1' and G_1'' computed by the Rheology Advantage software. The main drawback is that there is no control over the numerical method used to compute the integrals 19 and 20.

1.2 Results and discussion

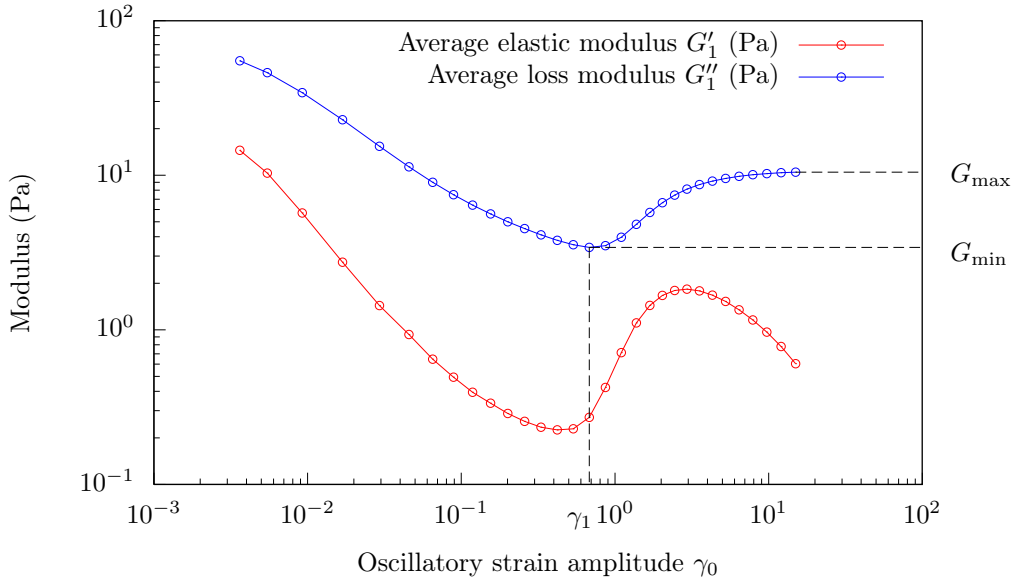

Figure 9: The generic shape of the curves $G_1'(\gamma_0)$ and $G_1''(\gamma_0)$. The curves plotted were obtained for a volume fraction of 0.434 and a frequency of 10 rad/s.

The Figure 9 presents the generic shapes of the curves $G_1'(\gamma_0)$ and $G_1''(\gamma_0)$, with γ_0 the measured strain amplitude. This Figure was obtained for a volume fraction of 0.434 and a frequency of 10 rad/s, with different parameters than the protocol described earlier in order to show the general evolution of the loss modulus. The precision of the rheometer was not sufficient to observe the linear regime, which seems to happen for very low

strain deformation. We only see first what seems to be a shear thinning regime, where the loss modulus G_1'' and therefore the viscosity η_1' decrease with the strain amplitude. This regime is followed by a shear thickening regime, where the loss modulus increases with the strain amplitude. Finally, the loss modulus reaches a plateau for high strain amplitude. This generic shape defines two characteristic loss moduli: $G_{\min}$, defined as the minimum of the loss modulus between the shear thinning and shear thickening regimes, and $G_{\max}$, defined as the maximum of the loss modulus after the shear thickening regime.

I then measured these two characteristic moduli in function of the frequency and the volume fraction, using the protocol described in the previous subsection and octave scripts to automatically compute the minimum and maximum. The Figure 10 presents the values of $G_{\min}$ obtained for different frequencies at a volume fraction of 0.451. $G_{\min}$ is computed from both the ascendant and descendant sweeps. We see that there is a discrepancy between the two sweeps: I have found that the ascendant sweep is always lower than the descendant sweep, and that the longer the measurement is, the lower these curves are shifted. This discrepancy is diminished for lower volume fraction, until the two curves $G_{\min}(\omega)$ collapse on a same line crossing the origin. It was found that at a given volume fraction, the slopes of linear Least Mean Square (LMS) fits of the two curves $G_{\min}(\omega)$ were always comparable within the error bar. It was therefore assumed that this common slope is a viscosity η_- characterising a linear relation between $G_{\min}$ and ω when measuring during a sufficiently long time. If this assumption is false, then η_- can simply be interpreted as a typical value of the frequency-dependant viscosity $G_{\min}(\omega,\phi)/\omega$

$$\eta_-(\phi) = \lim_{\omega\to\infty} \frac{G_{\min}(\omega,\phi)}{\omega}. \tag{22}$$

While this quantity does not have an immediate physical interpretation, it allows us to get a frequency-independent viscosity, which will be useful in the following.

Similar observations were found for the maximum of the loss modulus $G_{\max}$. The comparable slopes obtained from the LMS fits of the curves $G_{\max}$ were used as values of the typical viscosity η_+, with

$$\eta_+(\phi) = \lim_{\omega\to\infty} \frac{G_{\max}(\omega,\phi)}{\omega}. \tag{23}$$

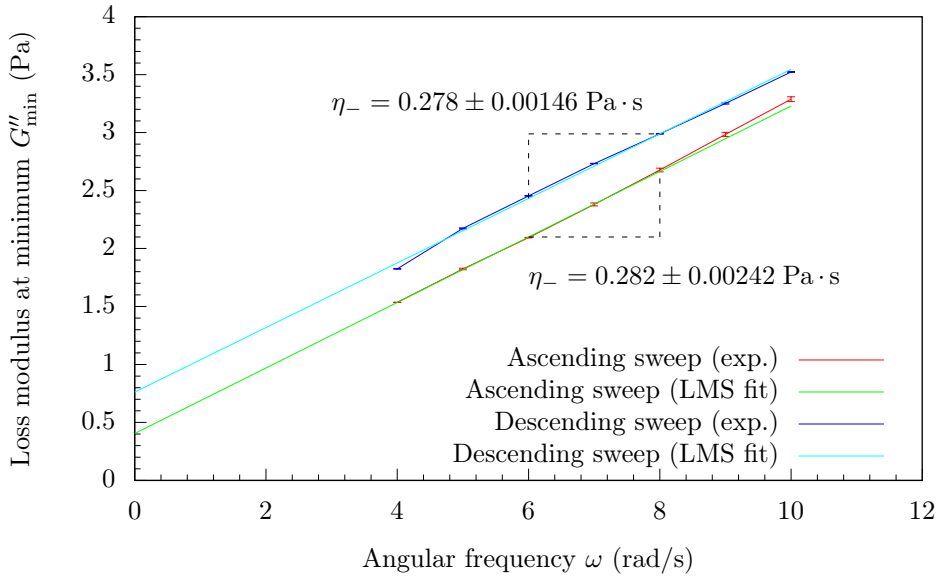

Figure 10: Values of $G_{\min}$, computed from both the ascendant and descendant sweeps, in function of the frequency ω, for a volume fraction of 0.451. The discrepancy between the two curves diminishes when increasing the duration of the sweeps, with the curves shifting down towards what seems a common linear relation between $G_{\min}$ and ω. At lower volume fraction, this discrepancy is less pronounced for the same duration of sweep

The Figure 11 presents the measured values of η_+ and η_- in function of the volume fraction ϕ, along with LMS fits using the generic divergence law $\eta_i/(1+\phi/\phi_i)^2$, with $i = 1, 2$. Two different jamming densities are found, similarly to the model of Wyart and Cates presented in the first part. But it should be noted that this double scaling happens for entirely different reasons: while with attractive suspensions, the crossover is guided by the number of contacts creating, with repulsive suspensions we don't have a repulsive force, and therefore contacts are always creating and destroying, whatever the stress level.

To understand a possible origin of this double scaling and the apparent shear thickening observed in LAOS experiment, we need to reinterpret these experiments in terms of shear reversal and structures. Indeed, there

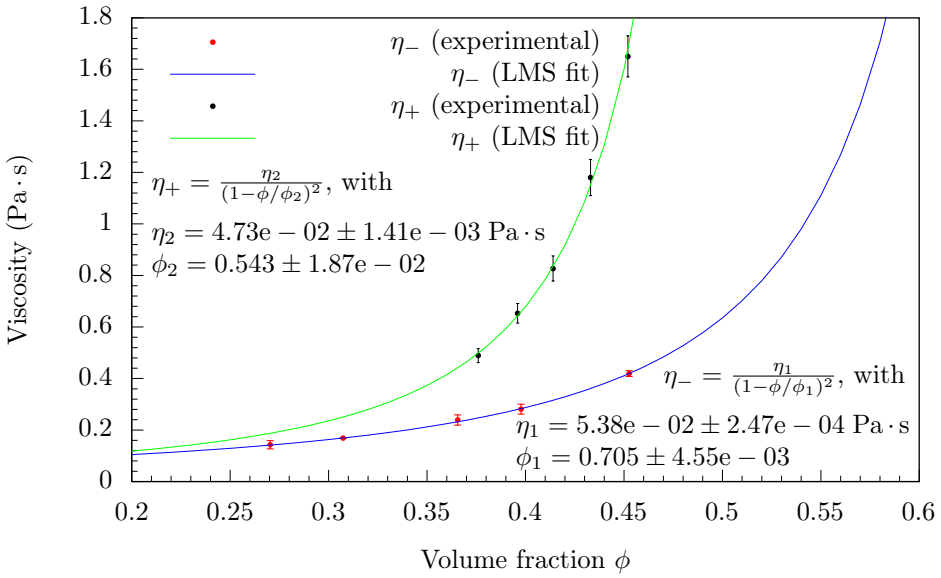

Figure 11: The scaling of η_- and η_+ in function of the packing fraction ϕ. The generic divergence law $\eta_i/(1+\phi/\phi_i)^2$ is used to fit the data with the Least Mean Square method, with $i = 1, 2$.

has been experimental [4] and theoretical [10] reports of a transient regime arising when the direction of shear is changed in dense suspensions or dry granular material: if a shear reversal is applied after the viscosity reaches a steady value η_∞, then the viscosity changes after and needs a typical strain deformation of a few unities before returning to its equilibrium value η_∞. This property can be interpreted in terms of anisotropy: for a purely isotropic fluid, the viscosity cannot depend on the direction of shear, because no anisotropy is created; on the contrary, if an anisotropy develops in one direction during a shear, we can expect a transient regime arising when changing the direction of shear, because the anisotropy has to change of sign.

As in a LAOS experiment, the direction of shear is constantly changing each half-period, we need first to understand what is happening during a pure shear reversal at $\|\sigma\|$ fixed in order to interpret the apparent shear thickening observed. This is the object of the next section, where shear reversal experiments are interpreted in terms of anisotropy and structures.

2 Shear reversal approach

First, how can we define an anisotropy in a suspension? If we define $\boldsymbol{n}$ as a vector representing a typical orientation in the fluid at the microscopic, then we can define the macroscopic tensor $\boldsymbol{A}$ as the following spatial mean over a mesoscopic domain (containing a sufficiently big number of particles) [5]

$$\boldsymbol{A} = \langle \boldsymbol{n} \otimes \boldsymbol{n} \rangle - \frac{1}{3}\boldsymbol{I}, \tag{24}$$

where $\boldsymbol{I}$ is the identity tensor. This symmetric and traceless tensor, somewhat similar to the nematic order parameter in a liquid crystal, is called fabric tensor (or anisotropy tensor). In the following, we will assume that $\boldsymbol{n}$ represents the direction between neighbouring particles. For purely isotropic suspensions (very dilute), $\langle \boldsymbol{n} \otimes \boldsymbol{n} \rangle = \boldsymbol{I}/3$ and therefore the fabric tensor is null. On the contrary, if an anisotropy develops under shear, it can be connected with a privileged direction $\boldsymbol{n}^*$, eigenvector associated with the biggest eigenvalue Λ^* of $\boldsymbol{A}$. For dry granular materials [10] and repulsive suspensions [9], this direction has been found to be approximately equal to the compression direction. We will assume the same behaviour for our attractive suspensions. The Figure 12 presents a schematic view of the structures associated with this anisotropy, in the form of ideal chains of forces crossing the samples.

Although the theoretical framework to develop a dissipative model of a viscoplastic suspensions has been set by Goddard [5], I have not found in the literature any proposition of a microstructure evolution for these types of suspensions. In this section, the focus will be on the experimental point of view: I will present the results of my shear reversal experiments with cornstarch in oil, and try to interpret these results with a possible qualitative microstructure evolution. I have only realised viscosity measurements, but ultimately, imaging techniques and/or simulations are needed to fully understand the microstructure.

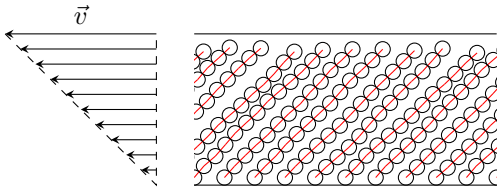

Figure 12: A simplified view of the structures arising during a shear in a suspension. These structures are sketched by perfect chains of forces across the samples, in the compression direction.

2.1 Experimental protocol

The same experimental setup as before is used, and samples are prepared as described in the previous section. Once the sample is loaded in the plate-plate geometry, a pre-shear at a high stress is applied during 1 hour before doing any measurements. The reason of this is that I have observed that under a shear, the viscosity of my attractive suspensions decreases continuously over a very long time scale, in agreement with the observation of Gadala-Maria and Acrivos [4] in suspensions of solid spheres. The viscosity decreases quickly just after the loading, and it slows down significantly after one hour. Therefore, the pre-shear allows us to have a more stable viscosity at equilibrium. After this pre-shear, the following protocol is applied:

1. A value of stress $\sigma_0 > 0$ is chosen.
2. The stress $-\sigma_0$ is applied during a time $\Delta t = 10$ min, which was found sufficient to reach an equilibrium, and the strain is measured at the same time. A *fast sampling* option is chosen, which allows to decrease the sampling rate in a stepwise fashion from 1000 samples per second initially to 1 sample per second after 40 seconds.
3. After a software and hardware delay $\tau < 1$ s, the stress σ_0 is applied during the same time Δt, with the same *fast sampling* option.
4. A new value of stress σ_0 is chosen and we start again from step 2.

In the following, only the strain series measured during each positive creep (step 3, after shear reversal) are considered. I have checked that these strain series are not affected by the delay between the step 2 and 3: for an artificial delay $\tau = 1$ min, it was found that the strain series is modified by less than one percent. The origins of time and strain are fixed immediately after the positive creep begins. This protocol is summarized on Figure 13.

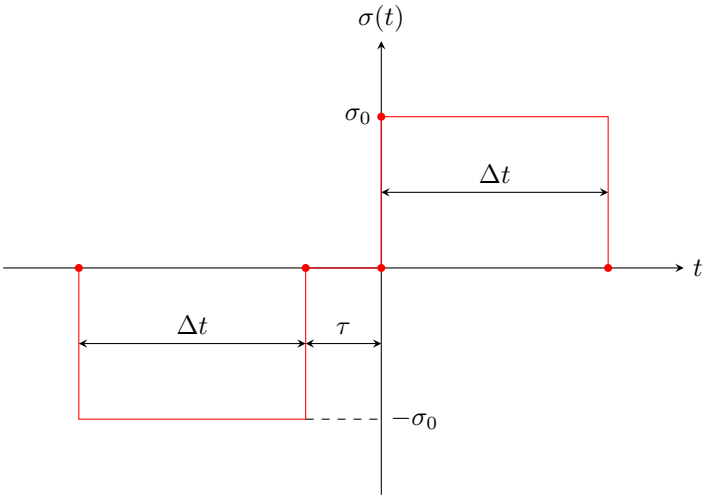

Figure 13: The stress pattern used to measure the viscosity after a shear reversal. Only the strain measurements for $t > 0$ are kept for further analysis. As the strain is defined up to an additive constant, we can choose a null strain at the beginning of the second creep: $\gamma(t = 0) = 0$.

2.2 Results

The Figure 14 presents the results obtained when using the protocol described above with a sample of volume fraction $\phi = 0.48$ and with values of stress covering approximately three decades. Three different regimes can be observed: the first regime, above the yield stress $\sigma_y \simeq 14$ Pa, is when the strain rate reaches an equilibrium value after a sufficiently long time, which corresponds to a linear evolution of the strain. The second regime, between the yield stress σ_y and a lower typical stress $\sigma'_y \simeq 0.6$ Pa, consists in two typical strain plateau. The first strain plateau is around 10^{-4}, independently of the stress, and the second plateau, starting at 10 just below σ_y, is shifting down for lower stress. Finally, the third regime, below σ'_y, presents only one strain plateau, starting around 10^{-4} just below σ'_y and shifting down for lower stress.

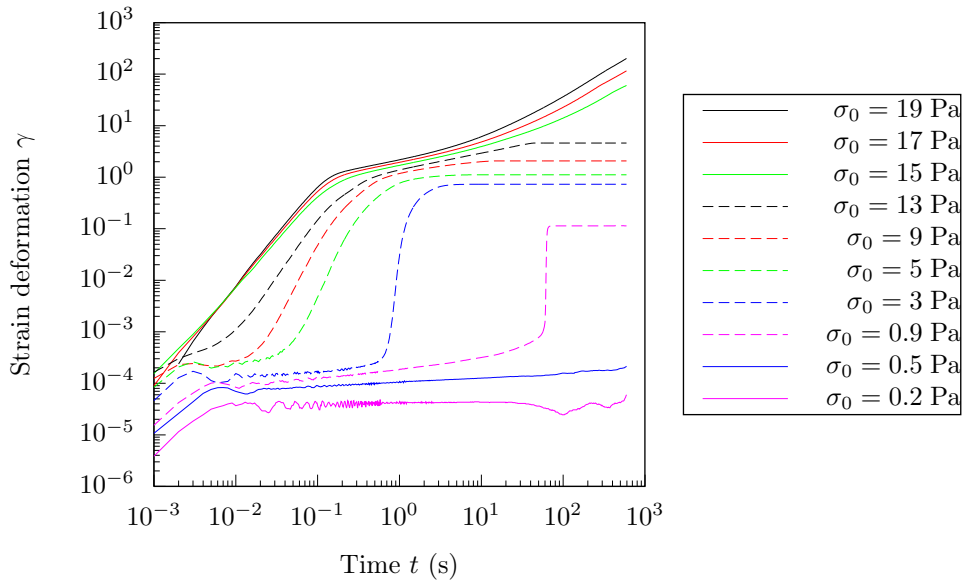

Figure 14: The strain series measured after a shear reversal for different values of stress. Decreasing stresses correspond to decreasing strain. Above the yield stress $\sigma_y \simeq 14$ Pa, the strain asymptotically tends to a linear evolution (the strain rate reaches an equilibrium value), while below the yield stress, the strain seems to tend to a fixed equilibrium value, or at least evolute very slowly.

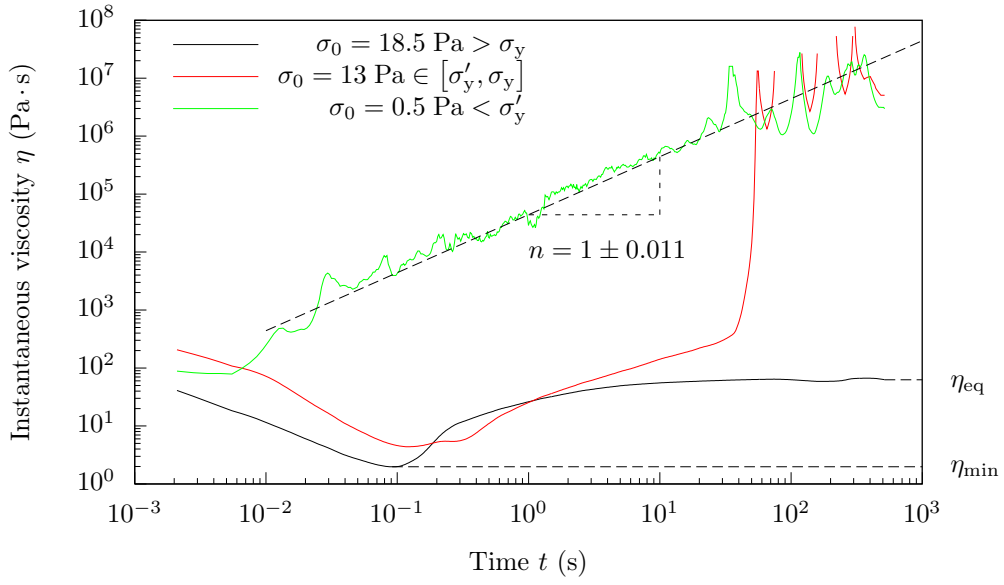

Figure 15: The instantaneous viscosity measured after a shear reversal for three typical stresses. After a long time, either the viscosity reaches an equilibrium value (above the yield stress) or diverges with the time (below the yield stress).

Plotting the strain in function of the time is not the best way to see if there is still a flow below the yield

stress. As an alternate representation of the data of Figure 14, the instantaneous viscosity is plotted in the Figure 15 for three different stresses in each regime described above. The strain rate has been computed as the difference quotient of strain/time. Below the yield stress σ_y (regime 2 and 3), it is confirmed that the sample doesn't strictly jammed, but ultimately acquires a viscosity diverging linearly with the time. Another remarkable feature is the well-defined minimum of the viscosity when the stress is above σ'_y (regime 1 and 2). This minimum corresponds to the steepest slope of the associated strain series in Figure 14 (which is kind of hard to determine in log-log scale, hence this representation).

For a particular value of stress $\sigma_0 > \sigma_y$ and volume fraction ϕ, I define the viscosity at equilibrium $\eta_{eq}(\sigma_0, \phi)$ as the temporal mean of the instantaneous viscosity during the last minute of the creep, and the viscosity at minimum $\eta_{min}(\sigma_0, \phi)$ as the minimum of the instantaneous viscosity, as depicted in Figure 15. I have found that the typical strain deformation associated with η_{min} is roughly independent of the stress σ_0 and has a value of $\gamma \simeq 0.5$.

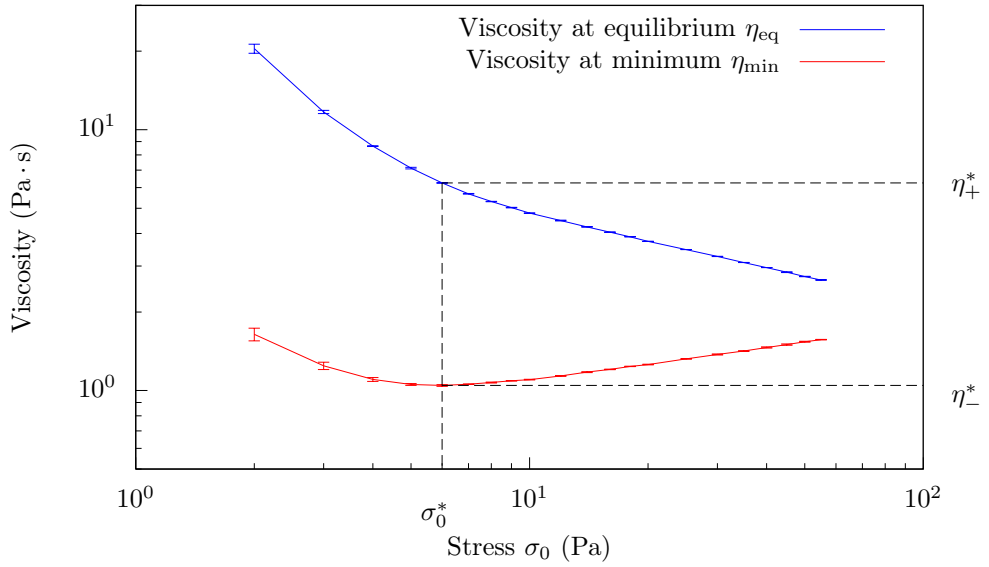

Figure 16: η_{eq} and η_{min} in function of the stress σ_0 at a packing fraction $\phi = 0.448$. Decreasing ϕ shifts down these two curves to lower stresses and viscosities, but the generic shape is kept. The position of the minimum of the function $\eta_{min}(\sigma_0)$ is used to construct two stress-independent viscosities, η^*_- and η^*_+

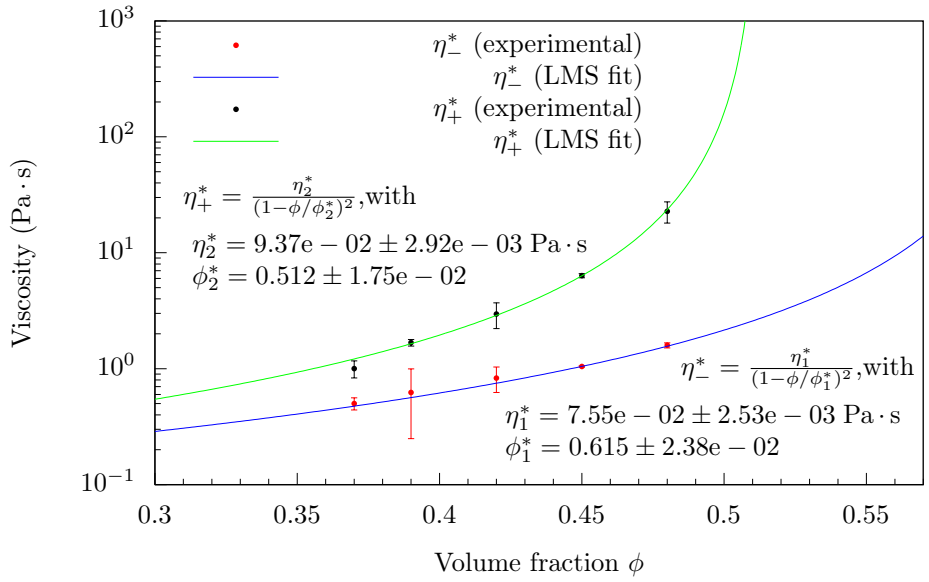

Figure 17: The scaling of $\eta^*_{-,+}$ in function of the packing fraction. The LMS fits corresponds to the same generic divergence law as before.

To see if η_{eq} and η_{min} possess an interesting scaling with respect to the packing fraction, I have measured these two functions for different values of ϕ and $\sigma_0 > \sigma_{\mathrm{y}}$. The Figure 16 presents the generic shape of η_{eq} and η_{min} in function of the stress σ_0 at a fixed volume fraction of $\phi = 0.448$. These curves are shifted to lower stresses and viscosities for lower packing fraction. To extract stress-independent values at fixed volume fraction, I define the following two viscosities

$$\eta_{-}^{*}(\phi) = \eta_{\mathrm{min}}(\sigma_0^{*}[\phi], \phi), \tag{25}$$

$$\eta_{+}^{*}(\phi) = \eta_{\mathrm{eq}}(\sigma_0^{*}[\phi], \phi), \tag{26}$$

where $\sigma_0^{*}(\phi)$ is the stress at which the function $\eta_{\mathrm{min}}(\sigma_0, \phi)$ is minimal at fixed ϕ, as depicted in Figure 16.

Finally, the Figure 17 presents the scaling of η_{-}^{*} and η_{-}^{*} in function of the packing fraction ϕ. Similarly to the previous section with the scaling of η_{-} and η_{+}, the two viscosities η_{-}^{*} and η_{+}^{*} diverge at two different packing fractions, respectively $\phi_1 \simeq 0.615$ and $\phi_2 \simeq 0.512$. These two volume fractions are a little lower than the two found in the LAOS experiment, but it should be noted that the quality of the LMS fits in Figure 16 is not as good as in Figure 11, and that a pre-shear was systematically applied before the shear reversal experiments, contrarily to the LAOS experiments.

2.3 Discussion

The similarities between the double scaling of the viscosity in LAOS and shear reversal experiments seem to indicate that the viscosity before shear thickening η_{-} is linked to the viscosity at the minimum after a shear reversal η_{min}, and that the viscosity after shear thickening η_{+} is linked to the viscosity at equilibrium η_{eq}. This can be understand in terms of typical strain deformations: as the minimum of the viscosity after a shear reversal always happens for a typical strain deformation of 0.5 (above the yield stress σ_{y}) or lower than 0.5 (between σ_{y}' and σ_{y}), we expect that the average viscosity of a LAOS experiment at a typical strain amplitude of 0.5 is dominated by the properties of η_{min}. Conversely, if the strain amplitude is sufficiently big $\gamma \gg 0.5$, we can expect that the viscosity at equilibrium η_{eq} will be explored during a LAOS cycle.

Now that a very basic link has been established between LAOS and shear reversal experiments, we still have to interpret the three types of transient regime observed in Figures 14 and 15. I have eventually come with an interpretation in terms of microstructure and anisotropy after fruitful discussions with Michiel Hermes and Mike Cates. The first thing that we need to assume is that the dissipation increases when anisotropy have formed in a material. This can physically be understood by looking at the very simplified representation of the structures in Figure 12: as the contacts are in majority oriented 'against' the flow, we can expect that at least the friction will increase the dissipation in the direction of the flow. Then we can interpret the transient viscosity of regime 1 (above the yield stress σ_{y}) in Figure 15 as a destruction/construction process: immediately after the shear reversal, the viscosity decreases because the structures formed in the other direction are destroying, until a minimum is reached for a typical strain deformation of 0.5 (all structures destroyed); after this minimum, the viscosity increases because the structures are reforming in the new direction, thus increasing the dissipation. Finally, the viscosity at the equilibrium η_{eq} is reached when all structures have formed in the compression direction. The Figure 18 resumes this process using the simplified representation of structures. The value of viscosity immediately after the shear reversal is not very well-defined on my experiments: sometimes it seems to be roughly the same as η_{eq}, which would indicate that the viscosity is continuous even if the stress is 'discontinuous' (we must take into account the feedback time scale), sometimes it seems to be greater than η_{eq}, which would indicate that the bonds between particles (Hamaker attractive force) need to be broken before destroying the structures. The sampling rate of the rheometer was not sufficiently high to allow more precise measurement, even by trying to stay as close as possible to the yield stress (maximised time scale).

For the regime 2 (between σ_{y}' and σ_{y}), the same interpretation can be kept, with only two differences: as the maximum accessible strain is lower and lower when decreasing the stress, I expect the structures to be only partially formed (which would correspond to a lower eigenvalue Λ^{*} in the fabric tensor); once these partial structures have reformed, the stress applied $\sigma \in \left[\sigma_{\mathrm{y}}', \sigma_{\mathrm{y}}\right]$ is not high enough to overcome the global friction forces induced by these structures, and therefore we obtain a creep flow with a viscosity diverging with time.

Finally, for the regime 3 (below σ_{y}'), there is no structures forming or destroying, because of the very small strain deformation accessible (less than 10^{-4}). In this regime, I expect the jamming to come from the Hamaker attractive force associated with the typical stress σ_{y}'. As $\sigma < \sigma_{\mathrm{y}}'$, this attractive force ultimately prevents the creation of a steady flow, and yields the same creep flow as regime 2.

Assuming that this interpretation is accurate, we can understand our attractive suspension as a *double yield stress fluid*. The first yield stress σ_{y}' is purely set by the Hamaker attractive force, and corresponds to a maximum strain deformation of roughly 10^{-4} just below σ_{y}' or lower for lower stresses. The second yield stress σ_{y} is purely set by the friction force arising from the anisotropy in the fluid, and corresponds to a maximum strain deformation of roughly 0.5 just below σ_{y} or lower for lower stresses. With this in mind, we can provide the following interpretation for the LAOS results: the linear regime at very low amplitudes corresponds to random contacts across the sample (no anisotropy); the shear-thinning regime corresponds to the progressive

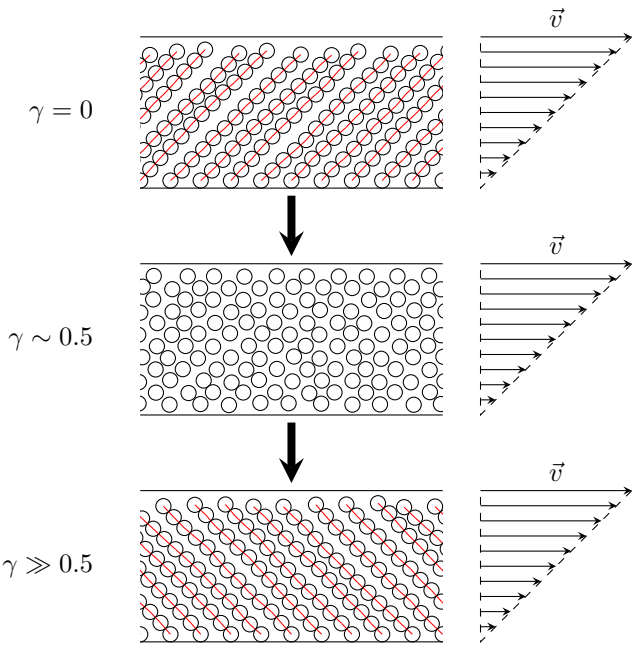

Figure 18: The creation/destruction process which could explain the transient regime of the viscosity above σ_y. For $\gamma < 0.5$, the structures are destroying, thus lowering the dissipation, while for $\gamma > 0.5$, the structures are recreating in the other direction, thus increasing the dissipation.

breaking of these contacts as the strain amplitude increases; finally, the shear thickening regime corresponds to the increasing importance of the structures forming and destroying (to do so, a minimum typical strain of 0.5 is needed, which corresponds to the strain amplitude at the minimum of the loss modulus).

Conclusion

I had the opportunity to explore the rheological properties of two different types of suspensions during this internship. The first type of suspension, cornstarch in solution of water in glycerol, presents both continuous and discontinuous shear thickening. The experimental flow curves include some features compatible with the recent model developed by Wyart and Cates [11], where the shear thickening is explained by a crossover between a frictionless physics at low stress (the repulsive force between particles is never overcome) and a frictional physics at high stress (the repulsive force becomes negligible and frictional contacts account for a high dissipation). These compatible features are the following: discontinuous shear thickening appears at a small range of volume fraction below a characteristic fraction ϕ_r; below ϕ_r, the high-viscosity plateau is always reached for a typical stress of 400 Pa independent of the volume fraction; above ϕ_r, no stable high-viscosity plateau is observed; the discontinuous shear thickening is equivalent to a continuous increase of stress at a fixed strain rate when working with a mean stress control, a property which can be interpreted with the formation of vorticity bands. However, some observations could not be interpreted: the deformation of the interface is delayed to higher stress when the volume fraction switch from the CST regime to the DST regime; an irreversible deformation of samples is observed when measuring a complete flow curve, from the low-viscosity plateau to the high-viscosity plateau; the evolution of the stress above ϕ_r could not be interpreted, due to visible fracture at the edge of the sample and the absence of clue for the existence of a high-stress state. Visualization techniques is the next step to understand these effects, but for this, a new system has to be used as cornstarch is not transparent with confocal microscopy.

The second type of suspension, cornstarch in oil, presents an equivalent of shear thickening when doing LAOS experiment: the mean viscosity η_1' is increasing with the strain amplitude γ, which gives two characteristic viscosities $\eta_{+,-}$ diverging at two different volume fractions. This property can be interpreted in terms of shear reversal experiments, as the direction of shear is constantly changing. These experiments have shown that our suspensions can be understand as a double yield stress material: the first yield stress σ_y' is set by the attractive Hamaker force between particles, and the second yield stress $\sigma_y > \sigma_y'$ is set by the friction force between particles when structures have formed in the compression direction. A typical strain displacement of 0.5 is necessary for destroying the anisotropic structures after a shear reversal, and the destruction/creation process yields a

typical viscosity pattern: as the anisotropy accounts for a higher dissipation due to the frictional contacts, the destruction of structures after a shear reversal is associated with a decrease of the viscosity and the creation of structures in the other direction is associated with an increase of the viscosity. This pattern defines two typical viscosities $\eta^*_{+,-}$ which share with $\eta_{+,-}$ a similar scaling with the volume fraction. Therefore, the increase of η'_1 in LAOS experiments is understood as an increase of the anisotropy when the strain amplitude is higher than 0.5 and increases. This interpretation is purely qualitative; imaging techniques and theoretical work are necessary to improve the understanding of these shear reversal experiments.

Annexes

1 Calibration of the moment of inertia

Let I be the moment of inertia of the rotating part of the setup (for the first step of the calibration, this corresponds to only the air bearing; for the second step of the calibration, this corresponds to the system {*air bearing; shaft; upper plate*}). This rotating part is submitted to a torque Γ coming from the motor, and a friction ν coming from the air bearing. Let α be the angular displacement of the rotating part. Then, the angular momentum theorem gives us the evolution equation for this system

$$I\frac{\mathrm{d}^2\alpha}{\mathrm{d}t^2} = \Gamma - \nu\frac{\mathrm{d}\alpha}{\mathrm{d}t}. \tag{27}$$

Let us recall that the rheometer can apply an arbitrary Γ, and measure α at any time. To measure I, the following torque is applied

$$\Gamma(t) = \Gamma_0\theta(t), \tag{28}$$

with $\theta(t)$ the Heaviside step function. If the initial condition is $\mathrm{d}\alpha/\mathrm{d}t(0) = 0$, then the solution of the previous differential equation can be written

$$\frac{\mathrm{d}\alpha}{\mathrm{d}t} = \frac{\Gamma_0}{\nu}\left(1 - \exp\left[-\frac{\nu t}{I}\right]\right). \tag{29}$$

For sufficiently low time $t \ll I/\nu$, the angular velocity is linear in time and does not depend on the friction ν

$$\frac{\mathrm{d}\alpha}{\mathrm{d}t} \simeq_{t\ll I/\nu} \frac{\Gamma_0 t}{I}. \tag{30}$$

Knowing Γ_0 and measuring $\mathrm{d}\alpha/\mathrm{d}t(t)$, I is therefore easily deduced.

2 Calibration of the friction

The same system as the previous section is considered (moment of inertia I, torque Γ, friction ν and angular displacement α). The feedback loop between Γ and α is used to impose $\mathrm{d}\alpha/\mathrm{d}t(0) = \dot{\alpha}_0$, and no torque is applied for $t > 0$. Therefore, the solution of the equation 27 for $t > 0$ can be written as

$$\frac{\mathrm{d}\alpha}{\mathrm{d}t} = \dot{\alpha}_0 \exp\left(-\frac{\nu t}{I}\right). \tag{31}$$

For sufficiently low time, the angular velocity is linear in time

$$\frac{\mathrm{d}\alpha}{\mathrm{d}t} \simeq_{t\ll I/\nu} \dot{\alpha}_0\left(1 - \frac{\nu t}{I}\right). \tag{32}$$

Measuring $\mathrm{d}\alpha/\mathrm{d}t(t)$ is therefore sufficient to deduce ν if I has already been calibrated.

3 Calibration of the particle density of the cornstarch

We consider a suspension consisting in a mass m_{cf} of cornstarch occupying a volume V_{cf} and a mass m_{oil} of oil occupying a volume V_{oil}. The total mass of the suspension is m, the total volume is V. The conservation of volume allows us to write

$$\frac{1}{\rho} = \frac{V_{\mathrm{cf}} + V_{\mathrm{oil}}}{m}, \tag{33}$$

with $\rho = m/V$ the total density of the suspension. Defining $\rho_{\text{oil,cf}} = m_{\text{oil,cf}}/V_{\text{oil,cf}}$ as the densities of the two constituents, and using $V_{\text{cf}} + V_{\text{oil}} = m_{\text{oil}}/\rho_{\text{oil}} + m_{\text{cf}}/\rho_{\text{cf}}$, the previous equation is modified in

$$\frac{1}{\rho} = \frac{m_{\text{oil}}}{m}\frac{1}{\rho_{\text{oil}}} + \frac{m_{\text{cf}}}{m}\frac{1}{\rho_{\text{cf}}}, \tag{34}$$

which is rewritten using the conservation of mass in

$$\frac{1}{\rho} = \left(\frac{1}{\rho_{\text{cf}}} - \frac{1}{\rho_{\text{oil}}}\right)\varphi_{\text{cf}} + \frac{1}{\rho_{\text{oil}}}, \tag{35}$$

with $\varphi_{\text{cf}} = m_{\text{cf}}/(m_{\text{cf}} + m_{\text{oil}})$ the mass fraction of cornstarch.

The equation 35 allows us to easily measure $\rho_{\text{oil,cf}}$ by measuring the densities of suspensions with different mass fractions of cornstarch. Experimentally, I have prepared five suspensions of mass fraction 0.334, 0.248, 0.167, 0.0898, and 0 (pure oil), and measured their densities with a density meter DMA 4500 (Anton Paar). The oil used is sunflower oil from Sainsbury's, and the cornstarch used comes from Sigma-Aldrich (S4126). The Figure 19 shows the inverse of the density in function of the mass fraction for these five suspensions, and a linear LMS fit of these data using equation 35 with the constraint $\rho_{\text{oil}} = \rho\,(\varphi_{\text{cf}} = 0)$. The error of the instrument is assumed negligible, therefore no error bars are represented. The error on the estimation of ρ_{cf} is computed using the correlation matrix of the LMS fit. I have found $\rho_{\text{oil}} = 0.920$ g/cm^3 for the sunflower oil and $\rho_{\text{cf}} = 1.45 \pm 0.004$ g/cm^3 for the Sigma-Aldrich cornstarch. I have checked that the same values are obtained with the Sainsbury's cornstarch partially used in the second part.

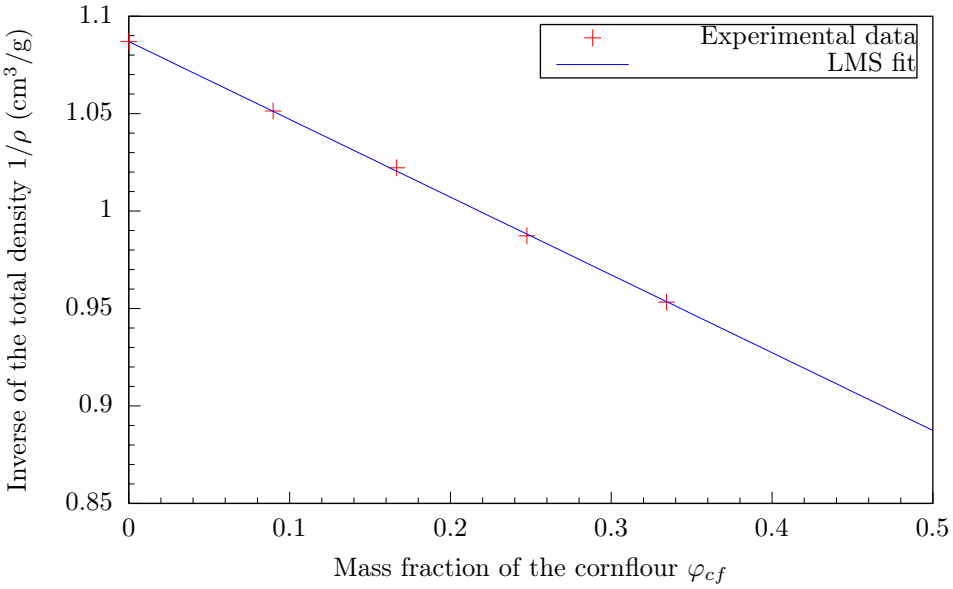

Figure 19: The inverse of the density plotted in function of the mass fraction. The equation 35 is used for the LMS fit.

References

[1] E. Brown and H. M. Jaeger. Shear thickening in concentrated suspensions: phenomenology, mechanisms, and relations to jamming. *arXiv preprint arXiv:1307.0269*, 2013.

[2] A. Einstein. Eine neue bestimmung der moleküldimensionen. *Annalen der Physik*, 324(2):289–306, 1906.

[3] R. H. Ewoldt, A. E. Hosoi, and G. H. McKinley. New measures for characterizing nonlinear viscoelasticity in large amplitude oscillatory shear. *Journal of Rheology*, 52(6):1427, 2008.

[4] F. Gadala-Maria. Shear-induced structure in a concentrated suspension of solid spheres. *Journal of Rheology*, 24(6):799, 1980.

[5] J. D. Goddard. A dissipative anisotropic fluid model for non-colloidal particle dispersions. *Journal of Fluid Mechanics*, 568:1, 2006.

[6] H. C. Hamaker. The london—van der waals attraction between spherical particles. *Physica*, 4(10):1058 – 1072, 1937.

[7] P. Oswald. *Rheophysics: the deformation and flow of matter*. Cambridge University Press Cambridge, 2009.

[8] W. B. Russel and D. Saville. *Colloidal Dispersions*. Cambridge University Press, 1992.

[9] R. Seto, R. Mari, J. F. Morris, and M. M. Denn. Discontinuous shear thickening of frictional hard-sphere suspensions. *Physical review letters*, 111(21):218301, 2013.

[10] J. Sun and S. Sundaresan. A constitutive model with microstructure evolution for flow of rate-independent granular materials. *Journal of Fluid Mechanics*, 682:590–616, 2011.

[11] M. Wyart and M. Cates. Discontinuous shear thickening without inertia in dense non-brownian suspensions. *arXiv preprint arXiv:1311.4099*, 2013.